State modulation in spatial networks with three interneuron subtypes

Madeline M. Edwards[1,2], Jonathan E. Rubin[1,3], and Chengcheng Huang[1,2,3,*]

[1]Center for the Neural Basis of Cognition, Pittsburgh, PA, USA
[2]Department of Neuroscience, University of Pittsburgh, Pittsburgh, PA, USA
[3]Department of Mathematics, University of Pittsburgh, Pittsburgh, PA, USA
[*]Correspondence: huangc@pitt.edu.

Abstract

Several inhibitory interneuron subtypes have been identified as critical in regulating sensory responses. However, the specific contribution of each interneuron subtype remains uncertain. In this work, we explore the contributions of cell-type specific activity and synaptic connections to dynamics of a spatially organized spiking neuron network. We find that the firing rates of the somatostatin (SOM) interneurons align closely with the level of network synchrony irrespective of the target of modulatory input. Further analysis reveals that inhibition from SOM to parvalbumin (PV) interneurons must be limited to allow gradual transitions from asynchrony to synchrony and that the strength of recurrent excitation onto SOM neurons determines the level of synchrony achievable in the network. Our results are consistent with recent experimental findings on cell-type specific manipulations. Overall, our results highlight common dynamic regimes achieved across modulations of different cell populations and identify SOM cells as the main driver of network synchrony.

Introduction

As animals navigate the environment, their nervous systems process and react to an ongoing bombardment of sensory information. Internal factors such as motivation, attention, expectations, and arousal strongly impact animals' perception, behavior and decision-making [1, 2, 3, 4]. Inhibitory neurons play an essential role in modulating the information processing and communication in cerebral cortex by tuning cortical oscillations, regulating the time window in which external inputs elicit cortical responses, and modifying the response gain of their excitatory counterparts [5, 6, 7]. Inhibitory neurons, however, cannot be considered as a homogeneous population, but instead exhibit differences in morphology, connectivity, and biophysical properties [8, 9]. Differences in molecular markers distinguish three non-overlapping inhibitory interneuron subtypes: parvalbumin (PV), somatostatin (SOM), and vasoactive intestinal peptide (VIP) expressing neurons. These interneuron subtypes are differentially targeted by neuromodulators and cortical feedback projections [9, 10, 11], and are thought to be involved in the modulation of neural population responses by brain state. Arousal and locomotion state of an animal have been shown to exert diverse influences on the firing rates of interneuron subtypes [12, 13, 14] and to strongly impact the synchrony level of neural population responses [15, 16]. However, the functional role of each interneuron subtype remains unclear.

Advancements in optogenetic techniques enable the use of cell-type-specific stimulation and suppression to study the causal contributions to circuit dynamics by each cell type. Prior work demonstrated diverse effects on cortical firing rates and oscillations elicited by manipulating different target cell classes within cortical microcircuits [6, 10, 17, 18, 19, 20]. Stimulating PV neurons periodically enhances the oscillatory

power of the local field potential (LFP) over the gamma frequency range [21, 22]. This is consistent with previous theories where PV neurons are instrumental in generating gamma oscillations, partly due to their strong reciprocal connections with the excitatory neurons [23]. However, recent work suggests that SOM neurons are involved in oscillations in low gamma/beta frequency range (20-40 Hz), while suppressing PV neurons increases the spectral power of the LFP overall [18, 24]. Suppressing SOM neurons also reduces the coherence between distant neural ensembles [24], consistent with their broad integration of lateral excitatory inputs [25]. Stimulating VIP neurons increases the response gain of excitatory neurons, presumably through the disinhibitory pathway via SOM neurons [26]. Silencing VIP neurons reduces the sensitivity of excitatory neurons to stimulus context [27] and increases the detection threshold for small visual stimuli [28]. Despite the proliferative experimental findings, the network mechanisms underlying the observed changes in neural activity remain elusive, due to the intrinsic nonlinearity of the highly recurrently connected networks to which all of these cell types belong. Manipulation of one cell type leads to changes in the activity of the other cell types; however, experimenters typically observe the activity of all neurons indiscriminately or label one cell type at a time (but see [29, 30]). Therefore, computational models are needed to parse out the interactions between excitatory neurons and the three interneuron subtypes.

Previous models that incorporate multiple interneuron subtypes mostly focus on modulations of firing rates and do not consider impacts on network synchrony or correlations in neural activity [31, 32, 33, 34, 35]. Some models have suggested that PV and SOM neurons contribute to oscillations of different frequencies [36, 37]. However, these models are small networks or rate models and do not consider the spatial dependence of synaptic connections. In this work, we studied state modulation in spatially structured spiking neuron networks including multiple interneuron subtypes. Our past work has shown that such models can reproduce the irregular and weakly correlated neural population activity commonly observed in cortical recordings [38]. We applied modulatory input to neurons of each cell type and analyzed the resulting changes in firing rates and network synchrony. We found that the pattern of activity changes resulting from activation of excitatory (E) or PV neurons is distinct from that due to activation of SOM or VIP neurons. Strikingly, SOM firing rates closely aligned with levels of network synchrony across all modulation cases. We further identified that stronger SOM→E than SOM→PV inhibition is important for maintaining a weakly synchronized dynamical regime, and that the interaction between E and SOM neurons is essential for enhancing network synchrony. Our work emphasizes the uniquely critical role of SOM neurons in regulating the dynamical state of cortical networks.

Results

We developed a spatially-extended network model that includes one E population and three distinct inhibitory interneuron populations: PV, SOM, and VIP. Each neuron is modeled as a spiking exponential integrate-and-fire (EIF) unit [39]. The synaptic connection patterns among the four neuron populations are constrained by anatomical and physiological data from mouse visual cortex (Figure 1A) [40, 41]. In particular, we assume there are no reciprocal connections among SOM neurons or among VIP neurons; VIP neurons mainly inhibit SOM neurons, in what is believed to be an important disinhibitory pathway [26]; and feedforward inputs only target E and PV neurons [25]. Neurons are randomly distributed on a two-dimensional plane and synaptic connection probability between neurons decays with distance (Figure 1B; Equation 5). The spatial structure of the network allows for rich spatiotemporal activity patterns, such as propagating waves and spatiotemporal chaos, with population statistics consistent with cortical recordings (Figure 1C, S2; Ref [38, 42]). Connections to and from the SOM cells have a larger spatial

footprint compared to other connections, which is thought to be involved in surround suppression in visual cortex [25, 43]. The synaptic timescales of inhibitory connections from SOM and VIP neurons are slower than that of connections from PV neurons, which is in turn slower than that of excitatory connections, constrained by physiological data from mouse visual cortex [44]. The network has a total of 50,000 neurons comprising 40,000 E, 4,000 PV, 4,000 SOM, and 2,000 VIP neurons, with the population size ratios following anatomical data from mouse cortex [45].

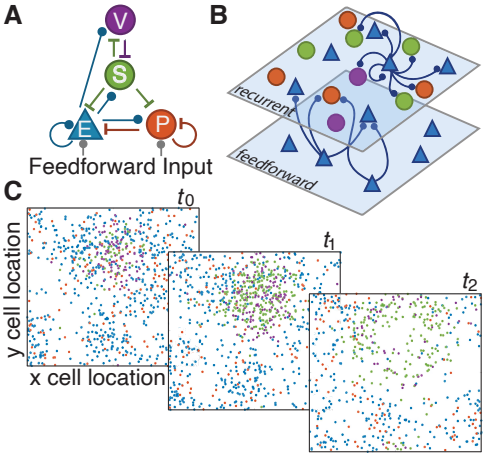

Figure 1: General model scheme and example dynamics. (A) Default network circuit diagram shows excitatory connections in blue (lines with circles) and inhibitory connections (T-lines) in other population-specific colors. (B) The model comprises one recurrent layer with one excitatory population and three inhibitory populations connected as in (A) and a feedforward layer, modeled as independent Poisson units, that provides excitatory input to E and PV neurons. Connection probability decreases with pairwise distance, as is illustrated schematically for E cells here. (C) Three consecutive spike raster snapshots, where a dot with a cell-type-specific color indicates that the neuron at spatial position (x, y) fired within 1 ms of the time stamp. In this example, local activity of E neurons (t_0) recruits more activity of SOM neurons at a later time point (t_1), which in turn suppresses the activity of all other neuron populations (t_2).

Network transitions through three dynamical states under variation of cell-type specific inputs

To begin our investigation, we apply a static input to each population in the model, one at a time, and examine network dynamics across a range of input levels. We find that across all input targets, the behavior of the network transitions through the same three distinct activity patterns, which we call the subcircuit asynchronous (SA), weakly synchronous (WS) and strongly synchronous (SS) states (Figure 2). We first define each state and then examine the effects of input modulation separately for each population. In the SA state (Figure 2Ai-iv; Supplemental video 1), the network behaves essentially as a two population subcircuit composed of interacting E and PV neurons, while SOM and VIP activity is nearly, if not completely, silent. The E population is the only excitatory source of input to SOM and VIP. In the SA state, E neurons are unable to consistently drive SOM and VIP neurons over their respective spiking thresholds (Figure 2Aii-iii). E neurons exhibit little synchronization or organized activity, as indicated by the near-zero levels of average spike count correlations between E neuron pairs (Figure 2Aiv). The average spike train coherence among E or among PV neurons is also low with a peak above 25 Hz (Figure 2Av).

Within the WS state, all four populations actively fire (Figure 2Bi-iv). PV neurons exhibit the highest firing rates, with the other three populations moderately active (Figure 2Bi-iii). The spiking activity of

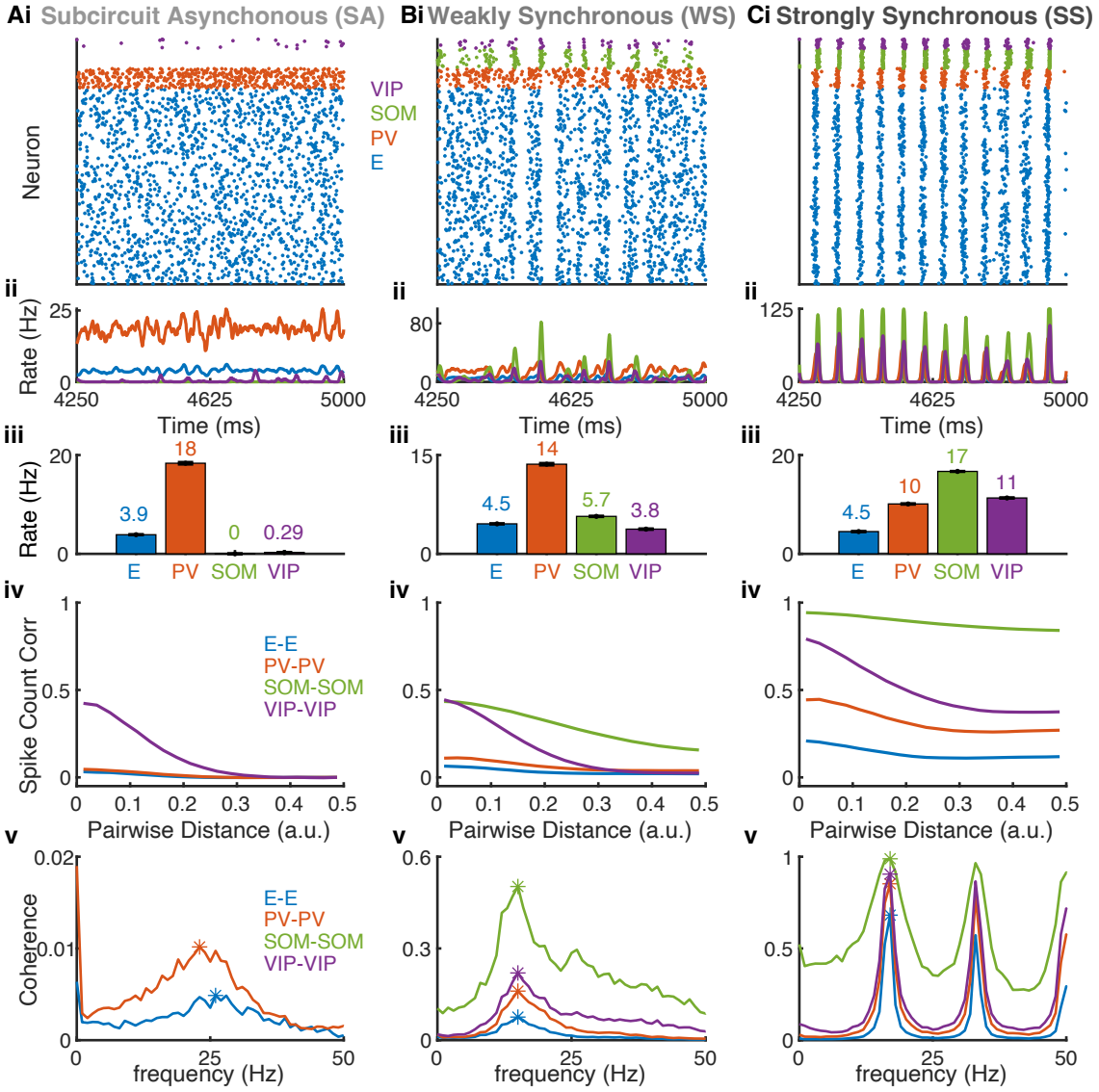

Figure 2: Three representative network states, SA state (Ai-v), WS state (Bi-v) and SS state (Ci-v). Row (i): Spike raster of a subsample of each of the four populations: 400 E (blue), 40 PV (red), 40 SOM (green), and 20 VIP (purple) neurons. The number of neurons of each neuron population shown in the rasters is proportional to the population size. Row (ii): Population-averaged firing rates over the same time course as the spike rasters in row (i). Row (iii): Mean firing rates averaged over neurons and over time for each population. The number on top of each bar is the value of the mean firing rate. Error bars are standard error of mean (SEM). Row (iv): Average spike count correlations (see Methods) as a function of distance for neuron pairs within each population. Row (v): Average pairwise coherence of spike trains (see Methods) versus frequency for neuron pairs within each population. The asterisks mark the maximum coherence over non-zero frequencies. Note the different y-axis scales across panels.

E and PV neurons is largely asynchronous, interspersed with brief coordinated periods of silence (Figure 2Bi; Supplemental video 2). The silent periods in E and PV are preceded by synchronous bouts of rapid firing in SOM and VIP neurons (Figure 2Bi,Bii). The spike count correlations and coherence of SOM-SOM and VIP-VIP neuron pairs are larger than those of E-E and PV-PV neuron pairs (Figure 2Biv-v), consistent with experimental observations in mouse cortex [44, 46]. The correlation between SOM neuron pairs persists over larger distances than those of other populations, due to the larger spatial footprints of SOM neuron connections, which is also consistent with cortical recordings [46].

The SS state exhibits highly synchronized and oscillatory activity in all populations (Figure 2Ci-iv). Patterns of firing initially begin with a low number of E and PV spikes, which recruit many more E and PV neurons to fire, thereby activating a large portion of SOM and VIP neurons (Supplemental video 3). The elevated firing rates of all three inhibitory populations (Figure 2Cii-iii) supply a significant amount of inhibitory current, ultimately silencing all neurons until enough feedforward input accumulates to excite E and PV neurons and to cause the cycle to repeat (Figure 2Ci). Pairwise spike count correlations are relatively large within each population and only slightly decrease with distance (Figure 2Civ). The average coherence of each neuron population shows a dominant peak close to 1 at around 20 Hz (Figure 2Cv). Since spike count correlations depend on the choice of time window for calculating spike counts, the correlation value can be misleadingly low when the time window coincides with the multiples of the oscillation period. For this reason, we hereafter use the maximum coherence to measure the level of network synchrony.

Comparing the effects of varying a static input current applied to different neuron populations reveals that external inputs to different targets modulate population dynamics across similar states. Specifically, we see that activating E neurons increases coherence in all populations (Figure 3A). As input to E increases, network activity transitions from the SA to the WS to the SS state. The transition is marked by non-monotonic changes in firing rates in E and PV populations (Figure 3Ai). The counterintuitive decrease of firing rate with increasing external input to E is due to the enhanced inhibition from SOM neurons. On the other hand, the firing rates of SOM neurons continue to rise despite reduced mean excitation from E due to the large increase in the temporal variance of the synaptic input currents they receive (Supplemental Figure S1Ai-ii).

In contrast, we see that increasing the external input to PV neurons results in a reverse order of state transitions compared to the case with input to E (Figure 3B). Activating PV neurons decreases coherence in population spiking, moving the network from the SS to the WS to the SA state. The firing rates of E and PV neurons again exhibit non-monotonic changes, as in the case with input to E neurons (Figure 3A). In the WS state, driving PV leads to increases in E firing rate because of the reduction in the inhibition from SOM neurons. The firing rates of SOM drop in the presence of increases in mean excitation due to the large reduction in the variance of input current (Supplemental Figure S1Bi-ii).

Driving SOM neurons increases population coherence and moves the network from the SA to the WS to the SS state, similar to the effects observed when driving E neurons (Figure 3C). However, the firing rates of E and PV neurons monotonically decrease as SOM neurons become more active (Figure 3Ci), in contrast to the non-monotonic changes that result when driving E or PV neurons (Figure 3Ai,Bi). VIP neurons become suppressed when SOM neurons are sufficiently activated due to inhibition from SOM to VIP (Figure 3Ci). In contrast, VIP and SOM firing rates co-vary in the same direction when input is applied to E or PV neurons (Figure 3Ai,Bi).

Lastly, varying the external input to VIP neurons yields similar changes to those arising with PV input variations, but is unable to induce all three of the network states that we have identified (Figure 3D). When input to VIP is strong, inhibition from VIP to SOM shuts down SOM activity and firing rates of E and PV

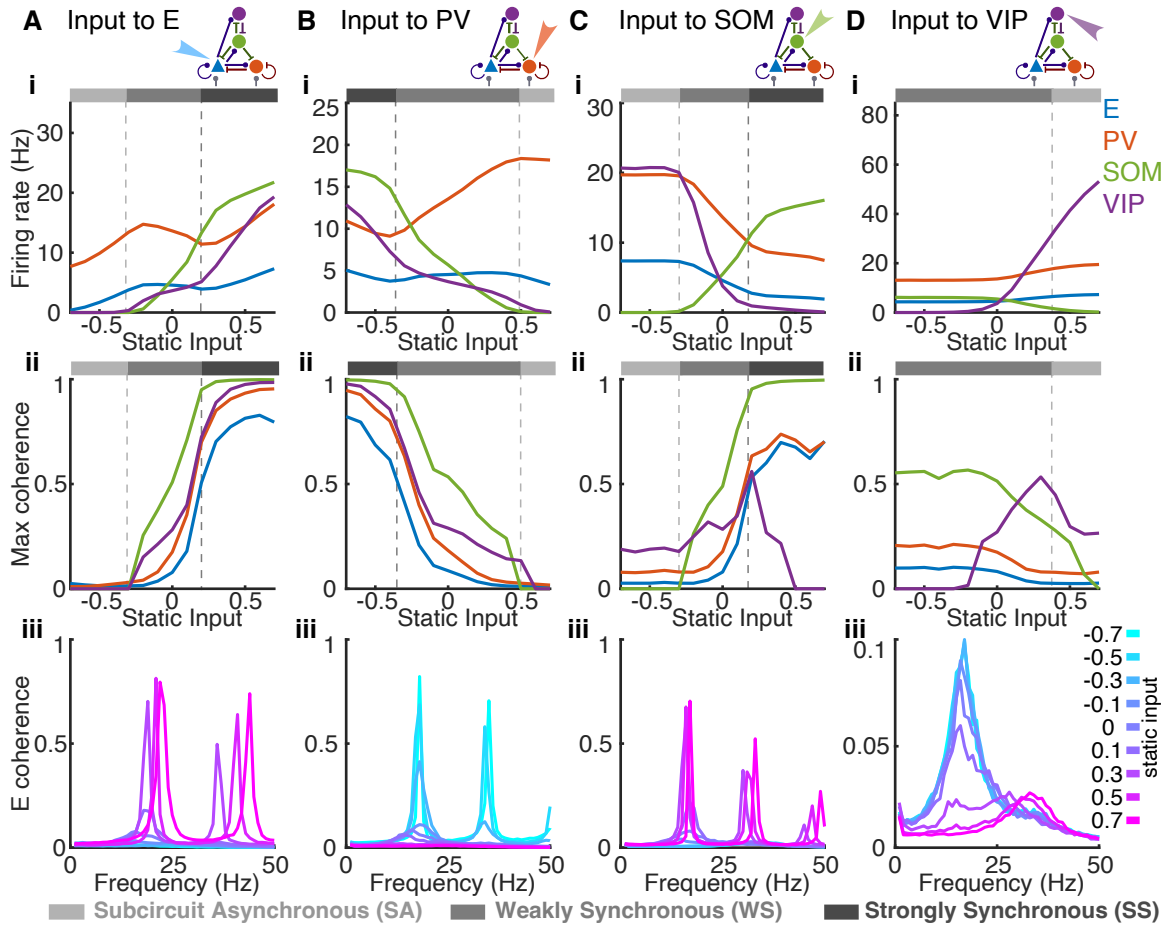

Figure 3: Cell type specific inputs change population firing rates and coherence in distinct ways. Static input is applied to all neurons in one of the four populations: (A) E, (B) PV, (C) SOM or (D) VIP neurons. Row (i): Average population firing rates of each population as a function of static input value. Grey-scale bars above each plot represent network activity state at the corresponding input value (SA: light grey; WS: moderate grey; SS: dark grey). Note the differences in vertical axis scales across panels. Row (ii): Maximum coherence in each population as a function of static input value. Row (iii): E population coherence as a function of frequency for several static input values. Note the distinct vertical axis scale in panel D(iii).

neurons increase slightly due to disinhibition. With SOM silenced and VIP having no synaptic connections to PV and E neurons, the network behaves asynchronously and effectively like a two population E-PV subcircuit, thus adopting the SA state. When input to VIP neurons is reduced, the drop in inhibition from VIP to SOM means that SOM starts to fire and VIP firing decreases. The network transitions from the SA to the WS state, and stays in the WS state once VIP neurons are fully suppressed (Figure 3Di, ii). Therefore, modulating VIP neurons does not lead the system to the pathological SS state, which makes the VIP neurons a ideal candidate for moderate state modulations. In addition, we observe that the frequency of peak coherence within the E population transitions (Figure 3Diii) as a result of changes in static input to VIP neurons. Activating VIP results in peak frequencies occurring at around 30 Hz, but as VIP reduces its activity due to reduced input and SOM begins to fire, the peak frequency shifts to approximately 20 Hz, with higher peak levels of E coherence.

We find that the spatial structure in the network is important for gradual state transitions, consistent with the observations in our previous work [38]. In networks with no spatial structure, meaning that the connection probability between two neurons does not depend on distance, we observe sharp transitions between SA and SS states as external input varies (Supplemental Figure S2Ai-iv). Therefore, the spatial structure of the network contributes to maintaining a WS state over a range of input values.

In all input cases, we observe similar network state for a given input in multiple simulation runs with random initial conditions. We also did not observe bistability when comparing network activity with gradually changing (increasing or decreasing) input (Supplemental Figures S7A,B). Based on the absence of hysteresis effects, we infer that the transition from the SA to the WS state likely occurs through a supercritical Hopf bifurcation.

Firing rates of SOM neurons co-vary with network synchrony

To directly compare how firing rates and network synchrony change together as input to each neuron population varies, we summarize the results of four input cases from the previous section with phase plots of the maximum coherence of the E population versus the firing rate of each neuron population (Figure 4). On these phase plots, each trajectory corresponds to a path of network state transitions as input to a specific neuron population varies. The arrows represent the directions of transition as input increases value. We use the maximum coherence of the E population to represent the overall network synchrony level for two reasons: first, E neurons make up the majority of the total neuron population (80%) and are recorded most commonly in experimental research and secondly, the coherence of all four populations tend to vary together, other than some exceptional results in VIP neurons (Figure 3A-Dii).

When plotting E population coherence versus E population firing rates, we find that for the cases of input to E or PV neurons, the network evolves along a common path, with opposite directions of traversal resulting from similar changes in static input levels (Figure 4A). Similarly, we obtain a common path for the cases of input to SOM or VIP neurons, but this common path differs from that observed with input to E or PV neurons. Previously we found that input to VIP never resulted in SS activity (Figure 4Dii), which explains why the VIP curve (purple) ends at a relatively low coherence value. Within the common path shared by E and PV stimulation, there exist three regimes: a lower branch where coherence is low (~ 0) and input changes only affect firing rate (the changing markers on the x-axis), an upper branch where coherence remains high (> 0.5) over a range of high firing rates, and a transition between the low and high coherence plateaus, across which coherence changes significantly while firing rates remain relatively unchanged. These regimes align with the network activity: the lower branch is the SA state, the upper branch is the SS state, and the transition is the WS state. What is especially remarkable is the precise

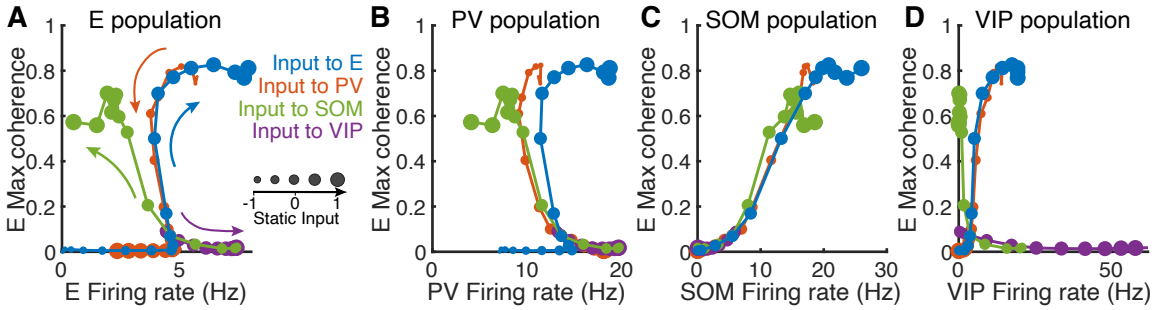

Figure 4: Modulation patterns of population firing rates and E population coherence. Levels of external input are indicated by individual circular markers, where decreasing marker size signifies decreased static input (i.e., progressing from activating to suppressing the target). Colors in each panel indicate which population receives the varying input and colored arrows (A) indicate the direction of increasing input (following the direction of increasing marker size along a single colored curve). Each panel depicts E coherence versus the population-averaged firing rate of one neuron population: (A) E, (B) PV, (C) SOM, and (D) VIP.

overlap of pairs of paths, along with the alignment of all paths during the transition region (i.e. the WS state), which suggests that the network structure strongly constrains network dynamics. The modulation patterns in the full network are distinct from those in the isolated E-PV subcircuit, where firing rate and coherence levels tend to vary in the same direction and monotonically as input level varies (Supplemental Figure S3).

Similarly, curves of E coherence versus PV firing rate overlap significantly for E and PV input cases, as do the curves for SOM and VIP input cases (Figure 4B). When comparing the E population coherence and SOM population rates (Figure 4C), however, the paths corresponding to application of static input to all four target populations largely overlap, no longer showing a distinction across input targets (aside from the direction of modulation across states as indicated by changes in marker sizes). Lastly, VIP firing rates compared to E coherence for all input cases (Figure 4D) features the dichotomy of trajectories generated by inputs to E and PV versus paths from inputs to SOM and VIP (as also observed in Figure 4A, B).

Overall, we see that applying excitatory input to E or SOM neurons or inhibitory input to PV or VIP neurons tends to increase coherence, although this change is accompanied by distinct changes in firing rates for most cell populations. Comparing SOM population rates with the coherence within the E population, however, reveals that the two quantities increase together, in a stereotyped way, in all input cases (Figure 4C). This consistency between E coherence and SOM activity across all input targets leads us to postulate that SOM activity plays a central role in dictating the level of network synchrony.

Strong SOM inhibition to PV drives synchrony

We next investigate how synaptic connection strengths in the network shape the modulation patterns of network states induced by cell-type specific inputs. Building on our prior observation of the alignment of SOM firing rate with network synchrony, we focus on the strengths of connections projecting onto or from SOM neurons, specifically SOM→E, SOM→PV, and E→SOM (next section) synapses. Since the influence of VIP's inhibitory outputs is restricted to SOM neurons, varying the connection strengths between VIP and SOM neurons has little effect on the input-induced transition patterns (Supplemental Figures S4 and S5).

We find that SOM→E connections are important for generating the non-monotonic changes in E and PV firing rates along the transition paths induced by varying input to E or PV neurons (Figures 3Ai,

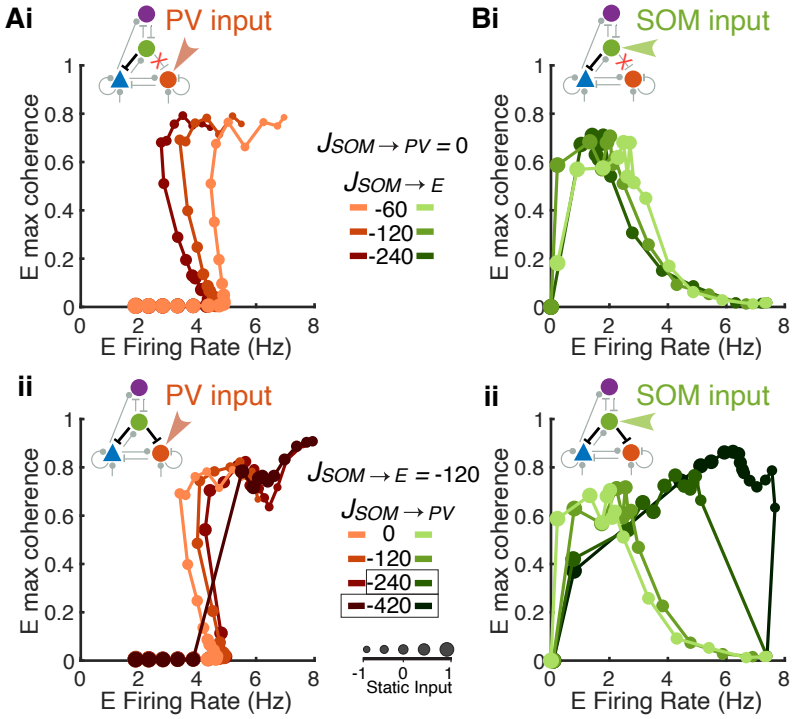

Figure 5: Relative strengths of SOM→E and SOM→PV connections shape modulation patterns of network state. Static input is applied to either PV neurons (Ai, ii) or SOM neurons (Bi, ii). Network state at each input level is represented by E firing rate and E maximum coherence (with the same convention as in Figure 4A). Increasing marker sizes correspond to increasing static input to the target population. (i) SOM inhibition to PV is removed ($J_{SOM\to PV} = 0$) and increases of $J_{SOM\to E}$ correspond to darker curves. (ii) SOM inhibition to E is fixed ($J_{SOM\to E} = -120$) and increases of $J_{SOM\to PV}$ correspond to darker curves. Default values of connections strengths are $J_{SOM\to E} = -120$ and $J_{SOM\to PV} = -60$.

Bi, and 4A). When we eliminate SOM→PV connections (i.e., $J_{SOM\to PV} = 0$), modulation patterns in network activity states (Figures 5Ai, Bi) remain qualitatively the same as in the network's default setting (Figures 3Bi, and 4Ai, Bi; more combinations of SOM→E and SOM→PV connection strengths are in Supplementary figure S6). Stronger SOM→E connections lead to a larger range of firing rates over the transition from the SA to the SS state through the middle branch, corresponding to the WS state, where rate and coherence vary in opposite directions (Figure 5Ai). The changes in state in response to external input variations are gradual in networks with different SOM→E connection strengths (Figure 5Ai, Bi). This points to a degree of resilience in the network's responsiveness to external input in the absence of SOM inhibition to PV.

This resilience is disrupted when the synaptic strength of SOM→PV dominates the synaptic strength of SOM→E, which results in an increased sensitivity of the network to changes in external input. Specifically, we consistently observe that when SOM inhibition to PV is sufficiently large compared to SOM inhibition to E, more pronounced and abrupt transitions from the SA to the SS state occur (e.g., the cases in Figure 5Aii with $J_{SOM\to PV} = -420$ and in Figure 5Bii with $J_{SOM\to PV} = -240, -420$; Supplemental Figure S6). That is, dominance of SOM→PV inhibition over SOM→E inhibition increases network sensitivity to input and reduces or eliminates the range of input levels that result in the transitional activity dynamics, the WS state. Indeed, in the transition through the WS state, as SOM firing intensifies (Figure 3i), the inhibition from SOM to E and PV neurons will tend to reduce their firing rates. Yet, the drop in PV firing can disinhibit E. If this disinhibitory effect is dominant due to sufficiently strong $J_{SOM\to PV}$, then E firing can increase rather than decreasing, resulting in a rapid transition through or elimination of the WS state. In this case, the firing rate and maximum coherence of E neurons tend to vary in the same direction (Figure 5ii, Supplemental Figure S6). Comparing results from increasing and decreasing incremental changes in input levels, we observe that the abrupt transition between SA and SS states happens at different input values depending on the direction of change (Supplemental Figure S7). This hysteresis effect suggests that stronger SOM inhibition to PV neurons changes the criticality of the Hopf bifurcation at which SA stability is lost, from supercritical to subcritical.

These results imply that stronger inhibition from SOM→E neurons than that from SOM→PV neurons is necessary to observe activity consistent with the WS state and underscores the pivotal influence of SOM inhibition on the network's dynamical transitions.

Dynamic interactions between E and SOM neurons are necessary for SOM-induced network synchrony

In this section, we investigate the impacts of E→SOM connections on SOM-induced network synchrony. What might drive the high coherence among SOM neurons and the rest of the newtork? Since SOM neurons do not connect to other SOM neurons and do not receive feedforward input, the high correlation among SOM neurons is driven by the recurrent input they receive from within the network. There are only two sources of recurrent inputs to SOM neurons, the excitation from E neurons and the inhibition from VIP neurons. To investigate the importance of E→SOM connections, we removed the E→SOM connections, and replaced this recurrent excitation with an external input that mimicked the statistics of the recurrent excitation.

First, we replaced recurrent excitation with colored noise that was independent for each SOM neuron. The colored noise was constructed as an Ornstein–Uhlenbeck (OU-) process that had equal mean and variance to the excitatory currents SOM neurons received on average in a intact default network with no static input (referred to as *baseline*; mean = 0.65 and variance = 0.12). In this decoupled network,

the coherence of the network remains low and decreases as we apply static input to SOM neurons, in addition to the noisy input, to increase their firing rates (Figure 6A). This result is opposite to the large increase in coherence with SOM rate that we observed in the default network (Figure 4A,C). The firing rate of E neurons is also suppressed much more abruptly compared to that in the default network as we increase input to SOM neurons (Supplemental Figure S8 compared to Figure 3C). This suggests that without E→SOM connections, SOM activity tends to reduce network synchrony mainly by reducing the E firing rate. The inhibition from VIP alone is not able to correlate SOM neurons. Consistently, varying VIP→SOM connections has little effect on network coherence (Supplemental Figure S5).

Next, we consider the possibility that correlated excitatory inputs are able to synchronize SOM neurons, which in turn synchronize the network as a whole. Because each SOM neuron receives input from a large number of E neurons (∼1200 connections), very weak correlation in E spike trains can result in large correlation in the pooled excitatory current, as has been demonstrated theoretically [47]. The correlated excitatory current to SOM neurons cannot be dynamically canceled by inhibition due to the lack of inhibitory connections among SOM neurons, which is distinct from the E-PV subcircuit where a balance of excitation and inhibition can be dynamically achieved [48, 49]. Therefore, excitatory input alone is able to drive correlated activity in SOM neurons. To demonstrate this, we record SOM spike trains from networks where SOM neurons receive excitation from E neurons but do not provide feedback inhibition to E and PV (Figure 6Bi, right column). Static input is applied to SOM neurons to modulate their firing rate. We then replay the recorded SOM spikes in networks where we remove E→SOM connections but allow SOM neurons to impact the rest of the network (Figure 6Bi, left column). In this way, E and SOM neurons are dynamically uncoupled, but SOM neurons receive realistic correlated excitation instead of simplified independent noise as in Figure 6A. We find that as input to SOM neurons increases, firing rate of SOM rises rapidly and their coherence level reaches to about 0.3 (Figure 6Bi, right column). This is consistent with the previous theoretical result that correlation between uncoupled neurons increases with firing rates [50]. The increased coherence in SOM spiking activity in turn induces synchrony among E neurons until E neurons are fully suppressed by the inhibition from SOM (Figure 6Bi, left column). Therefore, the correlated excitatory current to SOM neurons is able to drive the network into a weak synchrony regime (coherence around 0.15), but the peak coherence is much lower than that in the default network with E→SOM connections (Figure 6Bii).

Lastly, as we gradually restore E→ SOM connections ($J_{E\to SOM} > 0$) to allow for dynamic interaction between E and SOM neurons, we observe a positive relationship between the increases in coherence and increases in connection strength (Figure 6C). These results demonstrate that mimicking E→SOM input, using either colored noise with matched mean and variance (Figure 6A) or recorded SOM spikes from a decoupled network (Figure 6Bi-ii), is not sufficient to modulate activity through the three identified network states; rather, it is the dynamic interaction between E and SOM neurons that amplifies the weak correlation in the E-PV subcircuit and drives the network to strong synchrony.

Heterogeneous external inputs reduce SOM-induced network synchrony

In our previous set of results, adding noise to SOM neurons only slightly reduced the coherence of the network when E firing rate is small (Figure 6C, compare dark green with grey curves). This observation suggests that the network can still readily transition into a highly coherent regime even in the presence of noisy inputs that vary in time. To investigate the impact of noise in the external input, we applied independent OU input, with equal mean and variance, to each neuron in the SOM population (see Methods). Increasing the variance of the OU input only weakly impacted the coherence of the network (Figure

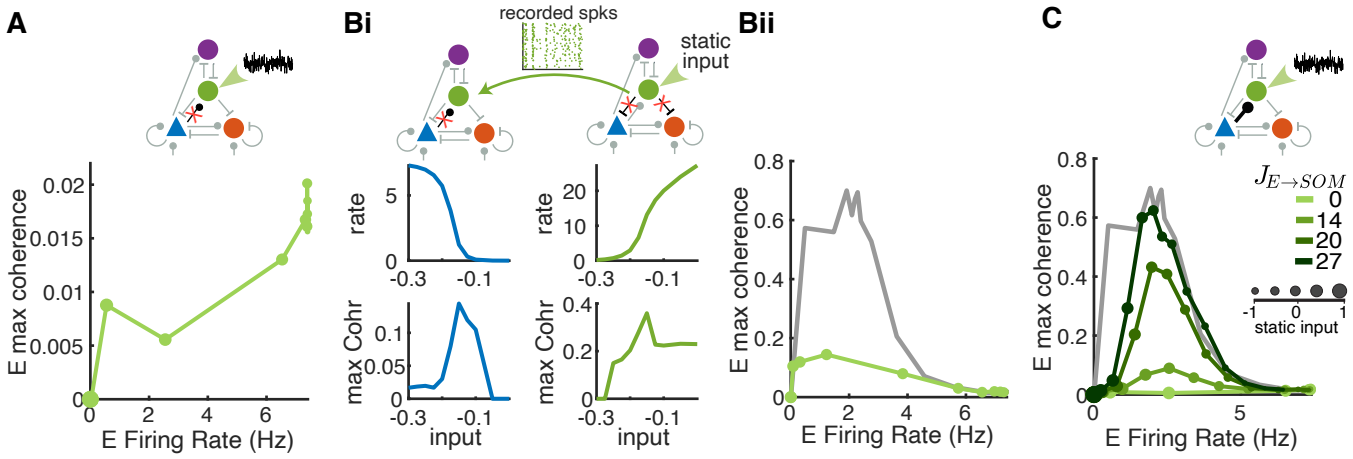

Figure 6: E→SOM connections are critical for SOM-induced network synchrony. (A) Removal of E→SOM connections eliminates coherence, despite the presence of stochastic input (OU process, see Methods) with mean and variance matched those of the excitatory currents to SOM neurons in the intact default network with no static input (mean = 0.65 and variance = 0.12). Larger dots correspond to stronger static inputs to SOM. (Bi-ii) E and SOM firing properties in networks where they are dynamically uncoupled, but SOM neurons receive and provide realistically correlated inputs and outputs, respectively. (Bi) Left column: Firing rate (top) and maximum coherence (bottom) of E neurons in networks with no E→SOM connection and where SOM spikes were replaced with those recorded from the network on the right. Right column: Firing rate (top) and maximum coherence (bottom) of SOM neurons in networks with intact E→SOM but no SOM→E and SOM→PV connections. Static input was applied to SOM neurons in the network on the right. (Bii) Modulation pattern of the firing rate and maximum coherence of E neurons from the network in Bi left (green) and from the default network (grey) with changes in static input to SOM neurons. (C) Increasing E→SOM synaptic strength increases the maximum coherence that can be achieved by varying static input to SOM neurons. SOM neurons receive the same OU noise as in panel A as $J_{E\to SOM}$ values are varied. Hence the lightest green curve ($J_{E\to SOM}$=0) is the same as that in panel A. As in panel Bii, the grey curve shows coherence for the default network with static input for comparison (same data as in Figure 4A green curve).

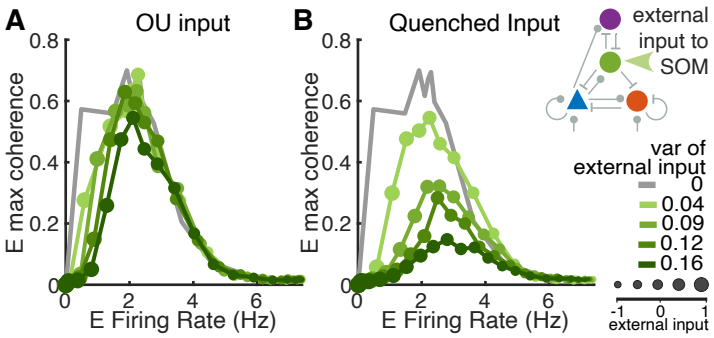

Figure 7: Comparison of two types of external input to SOM neurons. (A) Input to each neuron is modeled as an independent Ornstein–Uhlenbeck (OU-) process with the same mean and variance. (B) Input to each neuron is static in time but the strength is sampled independently from a normal distribution with a specified variance. The case of static input (variance equal to 0) is plotted in grey for comparison in each case (same as the grey curves in Figure 6).

7A). We next compared this outcome with the results of applying a different type of applied noise, heterogeneous or quenched noise, which is constant in time but has heterogeneous strengths, sampled from a normal distribution of a given variance, across target neurons (see Methods). Implementing the OU input and the quenched input allows us to compare the role of time-varying noise versus spatially-varying noise in terms of influence on coherence.

Interestingly, we find that quenched input to SOM neurons has a much larger impact on network synchrony than OU input with the same variance (Figure 7). With quenched input, we observe a substantial decrease in E coherence across most firing rates (Figure 7B). Across all cases of external quenched or OU inputs, the average population rates evolve similarly to the default network with homogeneous static input as input strength is varied (Supplemental Figures S9, S10). Firing rates change more gradually with increasing variance in the input, especially in the case of quenched input (Supplemental Figure S10). One difference across input types is that SOM is able to suppress E activity at lower values of quenched input than it can for static input. Overall, these results show that the transition to a synchronized network state resulting from enhancing the activation of SOM neurons is robust against time-varying noisy input that is of similar mean strength across the network, whereas a noise signal that has a spatially-varying strength is more effective at reducing the network synchrony level.

Discussion

In this study, using a spatially-structured spiking model of a canonical neural circuit comprising E, SOM, PV and VIP neurons, we demonstrate that SOM neurons are critical for synchronizing neural population activity. As external drive is varied to any target population, the firing rate of SOM neurons is highly predictive of the coherence level that emerges in the E population (Figure 4C). Without SOM neurons, network synchrony varies much more gradually with the level of input applied to the E-PV subcircuit (Figure S3). The spatial structure of the network is necessary for the gradual transition from asynchrony to strong synchrony via a weak synchrony state, because it allows for the richer spatiotemporal dynamics associated with this transitional regime, consistent with our past work ([38]; Figure S2). In addition, we find that when SOM→PV inhibition is strong, the smooth transition through the weak synchrony state is disrupted and the network becomes highly sensitive to input changes (Figure 5). We further show that the dynamic interaction between E and SOM neurons is a necessary factor in the emergence of SOM-induced

network synchrony, as a network in which E and SOM neurons are dynamically uncoupled remains in the asynchronous state even when SOM firing rate is high (Figure 6).

Our model reproduces previous experimental findings where optogenetic inactivation of SOM neurons led to a reduction in the oscillatory power of the LFP around 30 Hz while inactivation of PV neurons did the opposite (Figure 3; [18, 24]). Consistent with these experiments [18, 24], SOM neurons contribute to oscillations of lower frequency (∼20 Hz) and PV neurons contribute to oscillations of higher frequency (∼35 Hz) in our model, partly due the differences in their synaptic decay time constants (8 ms for PV and 20 ms for SOM; [44]). We identified that the firing rate of SOM neurons is tightly correlated with the overall network synchrony level (Figure 4C), which is also consistent with the previous experimental finding that the average activity of SOM neurons co-varies linearly with the gamma power of LFP (20-40 Hz) across multiple visual stimulus conditions (Figure S2 in [17]).

We find that the firing rate and coherence of E neurons can vary in opposite directions through the weak synchrony regime in networks with three interneuron subtypes (Figure 4A). In contrast, rates and coherence are tethered to vary in the same direction in the E-PV subcricuit (Figure S3). SOM neurons are responsible for the opposite relationship between rate and coherence of E neurons; when SOM neurons are more active, they suppress E neurons and increase network synchrony, and when SOM neurons are suppressed, E neurons firing rate increases and network synchrony is reduced. The opposite directionality of changes in E firing rates versus network synchrony has been observed with changes in spatial attention [51] and arousal state [15, 52]. The simultaneous increase in firing rate and decrease in synchrony can presumably enhance the signal-to-noise ratio of neural representations of stimuli [53]. Our results suggest that incorporating multiple interneuron subtypes supports the robust emergence of this enhanced coding state.

Our model predicts that a stronger or comparable magnitude of inhibition from SOM to E neurons compared to that from SOM to PV neurons is important for maintaining the weak synchrony regime (Figure 5, S6). When SOM to PV inhibition is much larger, the network shows abrupt transitions from the asynchronous to the strongly synchronous regime. This sensitivity arises because the positive feedback in the SOM→PV→E→SOM disinbitory loop can lead to instability. Our result is consistent with a previous model which suggests that SOM inhibition to PV neurons can result in a loss of stability [54]. The presence of stronger SOM inhibition onto E compared to PV neurons is in agreement with anatomical findings in cortex [40, 41, 55]. On the other hand, recent experimental work suggests that activating SOM neurons enhances the reliability of E neuron responses to natural movie stimuli by suppressing PV neurons [29]. The discrepancy between our model and this work could be due to the different temporal patterns of stimulation across the two. In our model, we only consider sustained application of external input, to model slow processes like the variation of brain state, while in these experiments [29], pulse stimulation was used. Further analysis is needed to investigate the dynamic responses of our model to brief, cell-type specific stimulation.

Our results also reveal an advantage of targeting VIP neurons to modulate a network's dynamical state. That is, targeting VIP neurons flexibly transitions the network between asynchronous and weakly synchronous regimes without pushing the network to pathologically strong oscillations (Figure 3). Anatomically, VIP neurons reside mostly in superficial layers in cortex and receive mostly long-range projections from other brain regions [9]. Therefore, they are hypothesized to be the main locus of feedback connections and neuromodulator release. VIP neurons also have been shown to respond strongly to locomotion signals [12], novel stimuli and unexpected events [56, 57]. Nevertheless, VIP neurons mainly act through SOM neurons to regulate the E-PV subcircuit. Therefore, it is the activity of SOM neurons that is mostly

reflective of network state in our model.

Our model mainly generates fluctuations with spectral power concentrated around 15-40 Hz. However, past work has shown that activation of SOM neurons reduces low-frequency power (<10 Hz) of LFP in addition to increasing high-frequency power [10]. Arousal state also tends to have opposing impacts on the low- versus high-frequency oscillatory power of LFP; high arousal state is associated with reduced power in the low-frequency band and increased power in the high-frequency band [15, 58, 52]. The lack of slow time-scale fluctuations in our model means that the model cannot fully account for the impacts of brain state on population activity. Future work is needed to extend the current model to consider various slow time variables, such as spike frequency adaption and slow synaptic receptors, that are omitted from the present work.

The brain features a vast diversity of neuronal types, each of which has unique connectivity patterns, expression of neuromodulator receptors and electrophysiological properties. Different cell types coordinate their activity to regulate neural population dynamics for flexible computations. Our model provides new insights and predictions about the different functions that each primary interneuron subtype may serve in modulating the dynamical state of cortex, highlighting the importance of E-SOM interactions and the relative strengths of SOM inputs to E versus PV neurons. Altogether, our results emphasize a unique role of SOM neurons in controlling network synchrony.

Methods

Spiking neuron network model

The model network consists of a single recurrent layer and a feedforward input layer (Fig. 1B). The feedforward layer (population X) is composed of 2,500 (N_X) excitatory neurons modeled as independent Poisson processes with a uniform rate of 10 Hz. The recurrent layer contains 50,000 neurons (N) divided into four cell population types, $N_e = 40,000$ E, $N_p = 4,000$ PV, $N_s = 4,000$ SOM, and $N_v = 2,000$ VIP neurons. The population size ratios follow anatomical data from mouse cortex [45]. The synaptic connection patterns among the four neuron populations are constrained by anatomical and physiological data from mouse visual cortex (Figure 1A; [40, 41, 25]). In particular, we assume there are no reciprocal connections among SOM neurons or among VIP neurons; VIP neurons only inhibit SOM neurons; and only E and PV neurons receive input from the feedforward layer (see Model parameters). Most of model parameters are similar to those in our previous work [38] except for some changes to incorporate different interneuron subtypes.

Each neuron in the recurrent layer is modeled as an exponential integrate-and-fire (EIF) neuron with membrane potential defined as:

$$C_m \frac{dV_j^\alpha}{dt} = -g_L\left(V_j^\alpha - E_L\right) + g_L \Delta_T e^{(V_j^\alpha - V_T)/\Delta_T} + I_j^\alpha(t), \tag{1}$$

where neuron j is a member of the α population, $\alpha \in \{e, p, s, v\}$. When $V_j^\alpha(t)$ exceeds a threshold V_{th}, the neuron spikes and the membrane potential is held at V_{th} for a refractory period τ_{ref} and then reset to a lower potential value, V_{re} (see Model Parameters). All membrane potentials are bounded below by $V_{lb} = -100$ mV. The total current to neuron j in population α is

$$\frac{I_j^\alpha(t)}{C_m} = \sum_{k=1}^{N_X} \frac{J_{jk}^{\alpha X}}{\sqrt{N}} \sum_n \eta_X(t - t_n^{X,k}) + \sum_{\beta=\{e,p,s,v\}} \sum_{k=1}^{N_\beta} \frac{J_{jk}^{\alpha\beta}}{\sqrt{N}} \sum_n \eta_\beta(t - t_n^{\beta k}) + \mu_\alpha + x_j(t), \tag{2}$$

where n indexes the spikes fired by the presynaptic neurons, $J^{\alpha\beta}$ is the recurrent synaptic strength from population β to population α (which may be 0 in some cases), $J^{\alpha X}$ is the synaptic strength from the feedforward layer to population α (see Model Parameters), μ_α is a constant external input current and $x_j(t)$ is input noise (Eq. 6). Note that the strength of each synaptic connection is scaled by $1/\sqrt{N}$. In equation (2), the postsynaptic current terms are defined as:

$$\eta_\beta(t) = \frac{1}{\tau_{\beta_d} - \tau_{\beta_r}} \begin{cases} e^{-t/\tau_{\beta_d}} - e^{-t/\tau_{\beta_r}}, & t \geq 0 \\ 0, & t < 0 \end{cases}, \tag{3}$$

where τ_{β_d} and τ_{β_r} (see Model Parameters) are the synaptic decay and rise time constants for population β. The synaptic timescales of inhibitory connections from SOM and VIP neurons are slower than that of connections from PV neurons, which is in turn slower than that of excitatory connections, constrained by physiological data from mouse visual cortex [44].

Neurons are uniformly distributed on a unit square, $\Gamma = [0, 1] \times [0, 1]$. The connection probability between a pair of neurons with coordinates $\mathbf{x} = (x_1, x_2)$ and $\mathbf{y} = (y_1, y_2)$, respectively, depends on the populations to which the neurons belong and the distance between the two neurons as

$$p_{\alpha\beta}(\mathbf{x}, \mathbf{y}) = \bar{p}_{\alpha\beta} g(x_1 - y_1; \alpha_\beta) g(x_2 - y_2; \alpha_\beta), \tag{4}$$

where $\bar{p}_{\alpha\beta}$ is the mean probability of connections from population β to population α and $g(x;\sigma)$ is a wrapped Gaussian distribution:

$$g(x;\sigma) = \frac{1}{\sqrt{2\pi\sigma}} \sum_{k=-\infty}^{\infty} e^{-(x+k)^2/(2\sigma^2)} \tag{5}$$

with projection width σ (see Model Parameters). Connections to and from the SOM cells have a larger spatial footprint compared to other connections, based on findings from mouse visual and auditory cortex [25, 43]. A presynaptic neuron is allowed to make more than one synaptic connection to a single postsynaptic neuron. The number of synaptic projections, or out-degree, $K_{\alpha\beta}$, from population α to population β is fixed for all neurons in population α, and indices of postsynaptic neurons are selected randomly according to the connection probability in Eq. 4.

For many of our simulations, the external input, μ_α, was varied between -1.0 and 1.0 with step size 0.1. Input noise, $x_j(t)$, was modeled as an independent Ornstein-Uhlenbeck (OU) process (Figures 6, 7):

$$\tau_{E_d} dx_j = (\mu_n - x_j)dt + \sigma_n dW, \tag{6}$$

where W is a Wiener process, and the time constant of the OU process was chosen to be the same as the decay time constant of the excitatory synaptic current, τ_{E_d}. The mean of $x_j(t)$ is μ_n and the variance is $\sigma_n^2/(2\tau_{E_d})$. In simulations where we replaced E→SOM connections with an OU process (Figure 6), we set $\mu_n = 0.65$ and $\sigma_n = 1.1$ to match the mean (0.65) and variance (0.12) of the excitatory current from E to SOM neurons in default networks without external input. In simulations with quenched input (Figure 7B), the constant external input, μ_j^α, to neuron j from population α is sampled from a normal distribution with mean μ_α and standard deviation Δ_μ.

The cellular parameters of the EIF model for each cell type and all network parameters are summarized in the Model Parameters section. The differential equations (1) and (2) were solved using a forward Euler method with a timestep of 0.05 ms. All simulations were performed on the CNBC Cluster at the Carnegie Mellon University. All simulations were written in a combination of C and MATLAB R2021b (9.11), MathWorks.

Model Parameters

The following tables specify the parameter values used in our simulations. As above, the symbol X denotes the feedforward connections.

Synaptic time constants

	E	PV	SOM	VIP	X
τ_d (ms)	5	8	20	40	5
τ_r (ms)	1	1	1	1	1

Synaptic connection strengths, $J_{\alpha\beta}$

		from (β)				
		E	PV	SOM	VIP	X
to (α)	E	30	-90	-120	0	120
	PV	40	-150	-60	0	250
	SOM	27	0	0	-10	0
	VIP	72	0	-10	0	0

Mean synaptic connection probability, $\bar{p}_{\alpha\beta}$

		from (β)				
		E	PV	SOM	VIP	X
to (α)	E	0.01	0.04	0.03	0	0.1
	PV	0.03	0.04	0.03	0	0.05
	SOM	0.03	0	0	0.1	0
	VIP	0.01	0	0.1	0	0

Number of postsynaptic connections, $K_{\alpha\beta}$

		from (β)				
		E	PV	SOM	VIP	X
to (α)	E	400	1600	1200	0	4000
	PV	120	160	120	0	200
	SOM	120	0	0	400	0
	VIP	20	0	200	0	0

Connection widths, $\sigma_{\alpha\beta}$

		from (β)				
		E	PV	SOM	VIP	X
to (α)	E	0.1	0.1	0.2	0	0.1
	PV	0.1	0.1	0.2	0	0.1
	SOM	0.2	0	0	0.2	0
	VIP	0.1	0	0.2	0	0

EIF Parameters

		E	PV	SOM	VIP
$\tau_m = \frac{C_m}{g_L}$	(ms)	15	10	10	10
τ_{ref}	(ms)	1.5	0.5	1.5	1.5
V_{lb}	(mV)	-100	-100	-100	-100
V_{th}	(mV)	-10	-10	-10	-10
Δ_T	(mV)	2	0.5	2	2
V_T	(mV)	-50	-50	-50	-50
V_{re}	(mV)	-65	-65	-65	-65
E_L	(mV)	-60	-60	-60	-60

Quantification and Statistical Analysis

Spike Count Correlations Spike counts were computed using a sliding window of 100 ms with a step size of 1 ms. Pearson correlation coefficients were computed for all neuron pairs as a function of distance (Figure 2iv), except that neurons with rates less than 1 Hz were excluded from correlation calculations. The membrane potential of each neuron was randomly initialized for each simulation, and connectivity matrices were regenerated for each input condition. A total of 5 simulations of 15 seconds each were performed for each input condition. The first 500 ms of each simulation was excluded from the analysis.

Coherence We measured the average pairwise coherence within each cell type population as an indication of network synchrony across simulation conditions. Spike trains were first partitioned into 1 ms time bins

and these were collected into 1 second time windows with 0.5 second overlap. Mean firing rate of each sampled neuron was subtracted. Power spectral density, S_i, of neuron i, and cross spectral density, S_{ij}, between neuron i and neuron j, were calculated using the fast Fourier transform and averaged over time windows. The coherence between neuron i and neuron j at frequency f was calculated as

$$C_{ij}(f) = \frac{S_{ij}(f)}{\sqrt{S_i(f)S_j(f)}}. \tag{7}$$

Pairwise coherence was averaged across all sampled neuron pairs within a population. Note that the coherence definition used here is not magnitude-squared, because the magnitude-squared coherence is always positive even when the network is asynchronous. We excluded neurons with rates less than 1 Hz and ensured that 500 neurons were sampled from each population. The first second of each simulation was removed.

Activity State Definitions We identified three network states that were observed for the range of input levels considered, based on mean firing rates and maximum coherence. Specifically, the subcircuit asynchronous (SA) state occurs when the average firing rate of SOM neurons is less than 1 Hz and the maximum coherence of E neurons is less than 0.1. The weakly synchronous (WS) state arises when the maximum coherence of E neurons is between 0.1 and 0.5 and the average firing rate of SOM neurons is larger than 1 Hz. The strongly synchronous (SS) state is when the maximum coherence of E neuron is larger than 0.5 and the average firing rate of SOM neurons is larger than 1 Hz.

Acknowledgments

M.E. received partial support by NIH grant T32NS086749. C.H. was supported by NIH grant R01NS121913, Simons foundation grant NC-GB-CULM-00002794-06, and the University of Pittsburgh. J.R. received partial support from NSF grant DMS1951095.

Author Contributions

M.E., J.R. and C.H. conceived the project; M.E. performed the simulations and analysis, in consultation with J.R. and C.H.; C.H. supervised the project; all authors contributed to writing the manuscript.

Data and Software Availability

Computer code for all simulations and data analysis will be available online upon publication.

Declaration of Interests

The authors declare no competing interests.

References

[1] Albright TD, Stoner GR. Contextual influences on visual processing. Annual review of neuroscience. 2002;25(1):339–379.

[2] Harris KD, Thiele A. Cortical state and attention. Nature reviews neuroscience. 2011;12(9):509–523.

[3] McCormick DA, Nestvogel DB, He BJ. Neuromodulation of Brain State and Behavior. Annual Review of Neuroscience. 2020;43(1):391–415.

[4] Flavell SW, Gogolla N, Lovett-Barron M, Zelikowsky M. The emergence and influence of internal states. Neuron. 2022;110(16):2545–2570.

[5] Isaacson JS, Scanziani M. How Inhibition Shapes Cortical Activity. Neuron. 2011;72(2):231–243.

[6] Cardin JA. Inhibitory Interneurons Regulate Temporal Precision and Correlations in Cortical Circuits; 2018.

[7] Ferguson KA, Cardin JA. Mechanisms underlying gain modulation in the cortex. Nature Reviews Neuroscience. 2020;21(2):80–92.

[8] Ascoli GA, Alonso-Nanclares L, Anderson SA, Barrionuevo G, Benavides-Piccione R, Burkhalter A, et al. Petilla terminology: nomenclature of features of GABAergic interneurons of the cerebral cortex. Nature Reviews Neuroscience. 2008;9(7):557–568.

[9] Tremblay R, Lee S, Rudy B. GABAergic interneurons in the neocortex: from cellular properties to circuits. Neuron. 2016;91(2):260–292.

[10] Chen G, Rasch MJ, Wang R, Zhang Xh. Experience-dependent emergence of beta and gamma band oscillations in the primary visual cortex during the critical period. Scientific Reports. 2015;5(1):17847.

[11] Zhang S, Xu M, Kamigaki T, Hoang Do JP, Chang WC, Jenvay S, et al. Long-range and local circuits for top-down modulation of visual cortex processing. science. 2014;345(6197):660–665.

[12] Fu Y, Tucciarone JM, Espinosa JS, Sheng N, Darcy DP, Nicoll RA, et al. A cortical circuit for gain control by behavioral state. Cell. 2014;156(6):1139–1152.

[13] Pakan JM, Lowe SC, Dylda E, Keemink SW, Currie SP, Coutts CA, et al. Behavioral-state modulation of inhibition is context-dependent and cell type specific in mouse visual cortex. Elife. 2016;5:e14985.

[14] Dipoppa M, Ranson A, Krumin M, Pachitariu M, Carandini M, Harris KD. Vision and locomotion shape the interactions between neuron types in mouse visual cortex. Neuron. 2018;98(3):602–615.

[15] Vinck M, Batista-Brito R, Knoblich U, Cardin JA. Arousal and Locomotion Make Distinct Contributions to Cortical Activity Patterns and Visual Encoding. Neuron. 2015;86(3):740–754.

[16] McGinley MJ, David SV, McCormick DA. Cortical Membrane Potential Signature of Optimal States for Sensory Signal Detection. Neuron. 2015;87(1):179–192.

[17] Veit J, Handy G, Mossing DP, Doiron B, Adesnik H. Cortical VIP neurons locally control the gain but globally control the coherence of gamma band rhythms. Neuron. 2023;111(3):405–417.e5. doi:10.1016/j.neuron.2022.10.036.

[18] Chen G, Zhang Y, Li X, Zhao X, Ye Q, Lin Y, et al. Distinct inhibitory circuits orchestrate cortical beta and gamma band oscillations. Neuron. 2017;96(6):1403–1418.

[19] Jang HJ, Chung H, Rowland JM, Richards BA, Kohl MM, Kwag J. Distinct roles of parvalbumin and somatostatin interneurons in gating the synchronization of spike times in the neocortex. Sci Adv. 2020;6(17).

[20] Wood KC, Blackwell JM, Geffen MN. Cortical inhibitory interneurons control sensory processing. Curr Opin Neurobiol. 2017;46:200–207.

[21] Cardin JA, Carlén M, Meletis K, Knoblich U, Zhang F, Deisseroth K, et al. Driving fast-spiking cells induces gamma rhythm and controls sensory responses. Nature. 2009;459(7247):663–667.

[22] Sohal VS, Zhang F, Yizhar O, Deisseroth K. Parvalbumin neurons and gamma rhythms enhance cortical circuit performance. Nature. 2009;459(7247):698–702.

[23] Buzsáki G, Wang XJ. Mechanisms of gamma oscillations. Annual review of neuroscience. 2012;35(1):203–225.

[24] Veit J, Hakim R, Jadi MP, Sejnowski TJ, Adesnik H. Cortical gamma band synchronization through somatostatin interneurons. Nature Neuroscience. 2017;20(7):951–959.

[25] Adesnik H, Bruns W, Taniguchi H, Huang ZJ, Scanziani M. A neural circuit for spatial summation in visual cortex. Nature. 2012;490(7419):226.

[26] Pi HJ, Hangya B, Kvitsiani D, Sanders JI, Huang ZJ, Kepecs A. Cortical interneurons that specialize in disinhibitory control. Nature. 2013;503(7477):521–524.

[27] Keller AJ, Dipoppa M, Roth MM, Caudill MS, Ingrosso A, Miller KD, et al. A Disinhibitory Circuit for Contextual Modulation in Primary Visual Cortex. Neuron. 2020;108(6). doi:https://doi.org/10.1016/j.neuron.2020.11.013.

[28] Ferguson KA, Salameh J, Alba C, Selwyn H, Barnes C, Lohani S, et al. VIP interneurons regulate cortical size tuning and visual perception. Cell reports. 2023;42(9).

[29] Rikhye RV, Yildirim M, Hu M, Breton-Provencher V, Sur M. Reliable sensory processing in mouse visual cortex through cooperative interactions between somatostatin and parvalbumin interneurons. Journal of Neuroscience. 2021;41(42):8761–8778.

[30] Potter C, Bassi C, Runyan CA. Simultaneous interneuron labeling reveals population-level interactions among parvalbumin, somatostatin, and pyramidal neurons in cortex. bioRxiv. 2024;.

[31] Litwin-Kumar A, Rosenbaum R, Doiron B. Inhibitory stabilization and visual coding in cortical circuits with multiple interneuron subtypes. Journal of Neurophysiology. 2016;115(3):1399–1409.

[32] Garcia del Molino LC, Yang GR, Mejias JF, Wang XJ. Paradoxical response reversal of top-down modulation in cortical circuits with three interneuron types. eLife. 2017;6:e29742.

[33] Palmigiano A, Fumarola F, Mossing DP, Kraynyukova N, Adesnik H, Miller KD. Common rules underlying optogenetic and behavioral modulation of responses in multi-cell-type V1 circuits. bioRxiv. 2020; p. 2020–11.

[34] Waitzmann F, Wu YK, Gjorgjieva J. Top–down modulation in canonical cortical circuits with short-term plasticity. Proceedings of the National Academy of Sciences. 2024;121(16):e2311040121.

[35] Beerendonk L, Mejías JF, Nuiten SA, de Gee JW, Fahrenfort JJ, van Gaal S. A disinhibitory circuit mechanism explains a general principle of peak performance during mid-level arousal. Proceedings of the National Academy of Sciences. 2024;121(5):e2312898121.

[36] Vierling-Claassen D, Cardin JA, Moore CI, Jones SR. Computational modeling of distinct neocortical oscillations driven by cell-type selective optogenetic drive: separable resonant circuits controlled by low-threshold spiking and fast-spiking interneurons. Frontiers in human neuroscience. 2010;4:198.

[37] Hahn G, Kumar A, Schmidt H, Knösche TR, Deco G. Rate and oscillatory switching dynamics of a multilayer visual microcircuit model. Elife. 2022;11:e77594.

[38] Huang C, Ruff DA, Pyle R, Rosenbaum R, Cohen MR, Doiron B. Circuit Models of Low-Dimensional Shared Variability in Cortical Networks. Neuron. 2019;101:337–348.e4. doi:10.1016/j.neuron.2018.11.034.

[39] Fourcaud-Trocmé N, Hansel D, Van Vreeswijk C, Brunel N. How spike generation mechanisms determine the neuronal response to fluctuating inputs. Journal of neuroscience. 2003;23(37):11628–11640.

[40] Campagnola L, Seeman SC, Chartrand T, Kim L, Hoggarth A, Gamlin C, et al. Local connectivity and synaptic dynamics in mouse and human neocortex. Science. 2022;375(6585).

[41] Pfeffer CK, Xue M, He M, Huang ZJ, Scanziani M. Inhibition of inhibition in visual cortex: the logic of connections between molecularly distinct interneurons. Nature neuroscience. 2013;16(8):1068.

[42] Mosheiff N, Ermentrout B, Huang C. Chaotic dynamics in spatially distributed neuronal networks generate population-wide shared variability. PLOS Computational Biology. 2023;19(1):e1010843.

[43] Kato HK, Asinof SK, Isaacson JS. Network-level control of frequency tuning in auditory cortex. Neuron. 2017;95(2):412–423.

[44] Karnani MM, Jackson J, Ayzenshtat I, Tucciarone J, Manoocheri K, Snider WG, et al. Cooperative subnetworks of molecularly similar interneurons in mouse neocortex. Neuron. 2016;90(1):86–100.

[45] Kim Y, Yang GR, Pradhan K, Venkataraju KU, Bota M, García del Molino LC, et al. Brain-wide Maps Reveal Stereotyped Cell-Type-Based Cortical Architecture and Subcortical Sexual Dimorphism. Cell. 2017;171(2):456–469.e22.

[46] Khoury CF, Fala NG, Runyan CA. The spatial scale of somatostatin subnetworks increases from sensory to association cortex. Cell Rep. 2022;40(10):111319.

[47] Rosenbaum R, Trousdale J, Josic K. Pooling and correlated neural activity. Frontiers in computational neuroscience. 2010;4:1209.

[48] Renart A, de la Rocha J, Bartho P, Hollender L, Parga N, Reyes A, et al. The Asynchronous State in Cortical Circuits. Science. 2010;327:587–590. doi:10.1126/science.1179850.

[49] Van Vreeswijk C, Sompolinsky H. Chaos in neuronal networks with balanced excitatory and inhibitory activity. Science. 1996;274(5293):1724–1726.

[50] De La Rocha J, Doiron B, Shea-Brown E, Josić K, Reyes A. Correlation between neural spike trains increases with firing rate. Nature. 2007;448(7155):802–806.

[51] Cohen MR, Maunsell JHR. Attention improves performance primarily by reducing interneuronal correlations. Nature Neuroscience. 2009;12(12):1594–1600.

[52] Reimer J, Froudarakis E, Cadwell CR, Yatsenko D, Denfield GH, Tolias AS. Pupil fluctuations track fast switching of cortical states during quiet wakefulness. neuron. 2014;84(2):355–362.

[53] Kohn A, Coen-Cagli R, Kanitscheider I, Pouget A. Correlations and Neuronal Population Information. Annual Review of Neuroscience. 2016;39(1):237–256.

[54] Bos H, Oswald AM, Doiron B. Untangling stability and gain modulation in cortical circuits with multiple interneuron classes. bioRxiv. 2008;doi:10.1101/2020.06.15.148114.

[55] Xu H, Jeong HY, Tremblay R, Rudy B. Neocortical somatostatin-expressing GABAergic interneurons disinhibit the thalamorecipient layer 4. Neuron. 2013;77(1):155–167.

[56] Garrett M, Manavi S, Roll K, Ollerenshaw DR, Groblewski PA, Ponvert ND, et al. Experience shapes activity dynamics and stimulus coding of VIP inhibitory cells. elife. 2020;9:e50340.

[57] Najafi F, Russo S, Lecoq J. Unexpected events modulate context signaling in VIP and excitatory cells of the visual cortex. bioRxiv. 2024; p. 2024–05.

[58] Akella S, Ledochowitsch P, Siegle JH, Belski H, Denman D, Buice MA, et al. Deciphering neuronal variability across states reveals dynamic sensory encoding. bioRxiv. 2024; p. 2024–04.

[59] Tsodyks MV, Skaggs WE, Sejnowski TJ, McNaughton BL. Paradoxical effects of external modulation of inhibitory interneurons. Journal of neuroscience. 1997;17(11):4382–4388.

[60] Ozeki H, Finn IM, Schaffer ES, Miller KD, Ferster D. Inhibitory stabilization of the cortical network underlies visual surround suppression. Neuron. 2009;62(4):578–592.

[61] Sanzeni A, Akitake B, Goldbach HC, Leedy CE, Brunel N, Histed MH. Inhibition stabilization is a widespread property of cortical networks. Elife. 2020;9:e54875.

Supplemental information

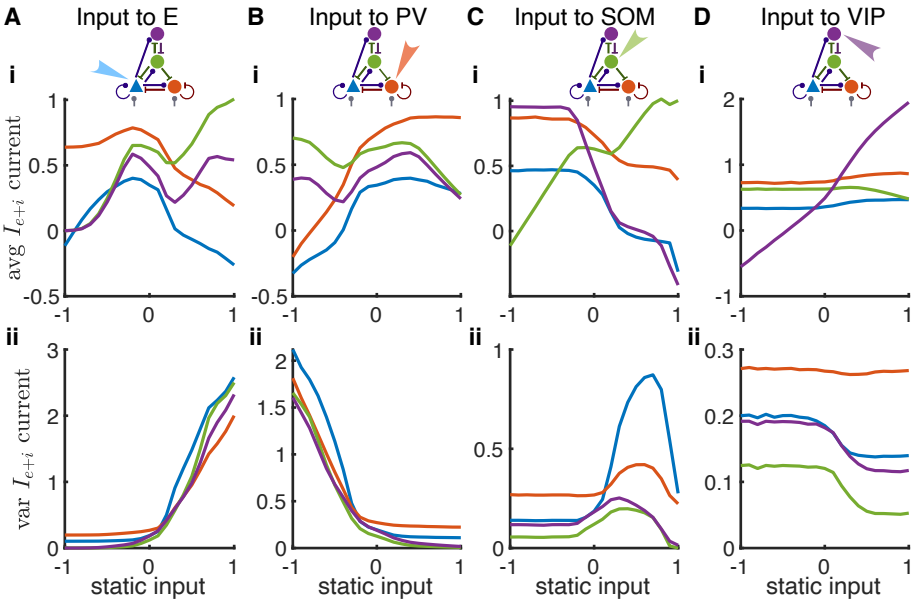

Figure S1: **Changes in synaptic currents as input is applied to each population. Related to Figure 3.** Static input is applied to the E (A), PV (B), SOM (C) or VIP (D) population. Row (i): Average total synaptic current to each population. Row (ii): Population-averaged variance of the total synaptic current to each population.

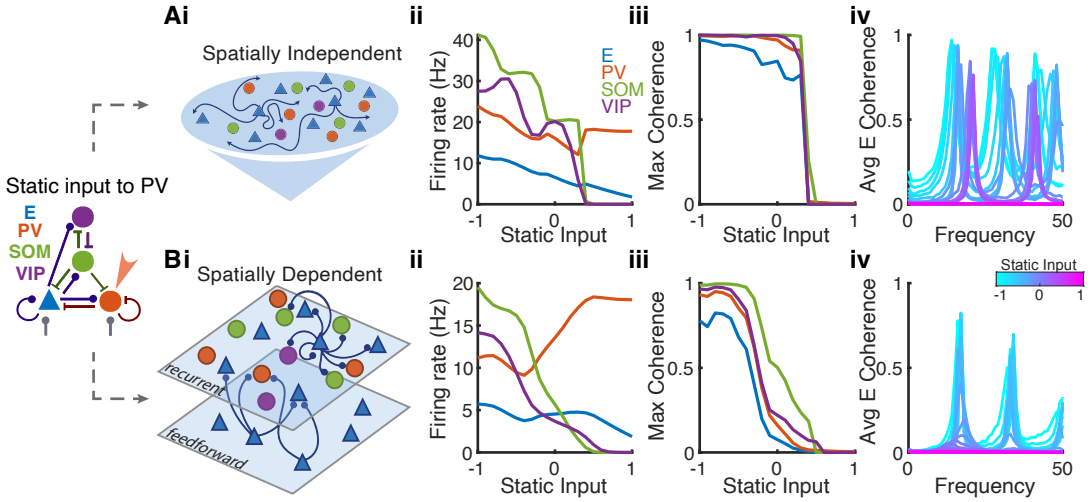

Figure S2: **Sharp transitions in networks with no spatial structure. Related to Figure 3.** Static input was applied to PV neurons. (Ai-iv) Firing rate and coherence in the four neuron populations in networks with no spatial structure, meaning that the connection probability between two neurons does not depend on distance. A sharp transition from the asynchronous to the strongly synchronous state occurs as input is increased. (Bi-iv) The same quantities for networks with spatial structure, as also shown in Figure 3B. The spatially dependent network exhibits a more gradual transition and the existence of weakly synchronous state over a range of input values. The parameters of the networks in A and B are the same except for the connection widths, $\sigma_{\alpha\beta}$ (see Model Parameters in Methods).

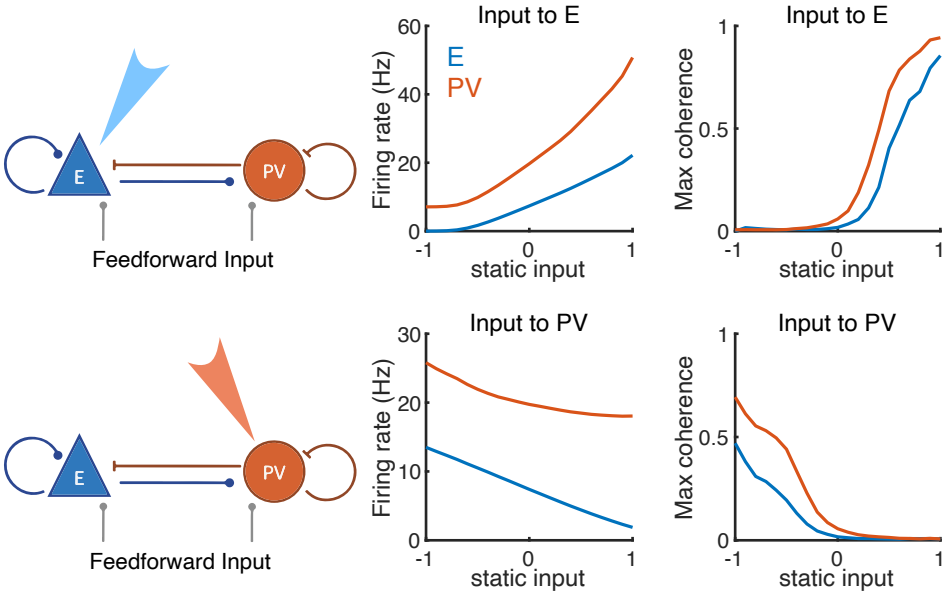

Figure S3: **Modulations of firing rates and maximum coherence in the E-PV subcircuit. Related to Figure 4.** Static external input was targeted to E (top row) or PV (bottom row) neurons. Firing rates and network synchrony are tethered to change in the same direction in the E-PV subcircuit. That is, stimulating E neurons increases the firing rates and coherence of both E and PV neurons, while stimulating PV neurons decreases firing rates and coherence in both populations. The paradoxical effect where stimulating PV leads to a reduction in PV firing rate suggests that the E-PV subcircuit is in the inhibition-stabilized regime [59, 60, 61]. Network parameters were the same as those Figures 1-4 except that we removed SOM and VIP populations.

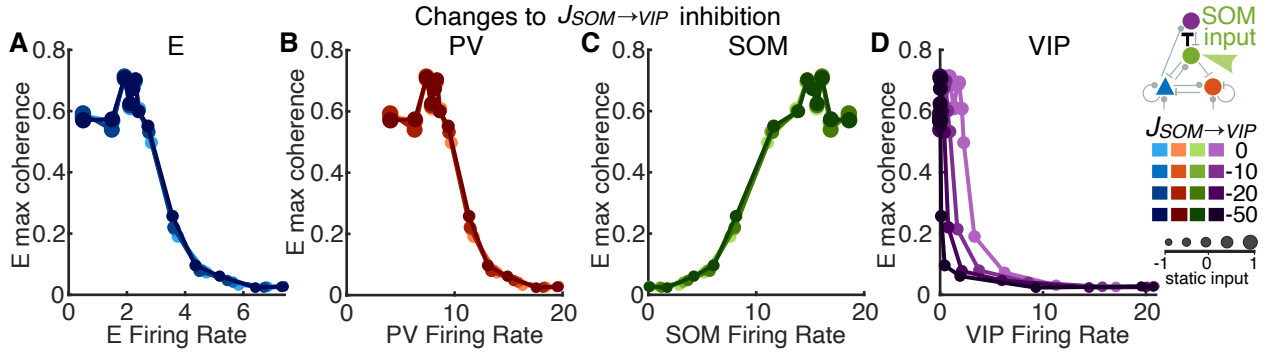

Figure S4: **SOM→VIP connection strength has little effect on modulation patterns. Related to Figure 5.** Static input was applied to SOM neurons.(A) E, (B) PV, (C) SOM, and (D) VIP population rates compared to E maximum coherence in networks with different SOM→VIP connection strengths, $J_{SOM\to VIP}$. Only the relation to VIP firing rate (panel D) is different in networks with different $J_{SOM\to VIP}$. In networks with larger $J_{SOM\to VIP}$ inhibition, SOM is able to suppress VIP at a lower rate, resulting in the darkened curves shifting leftward (D). Therefore, altering the connection strength of $J_{SOM\to VIP}$ exclusively affects the VIP population and does not influence how the rest of the network responds to external input. Note that $J_{SOM\to VIP} = -10$ is the default circuit parameter used in the main text.

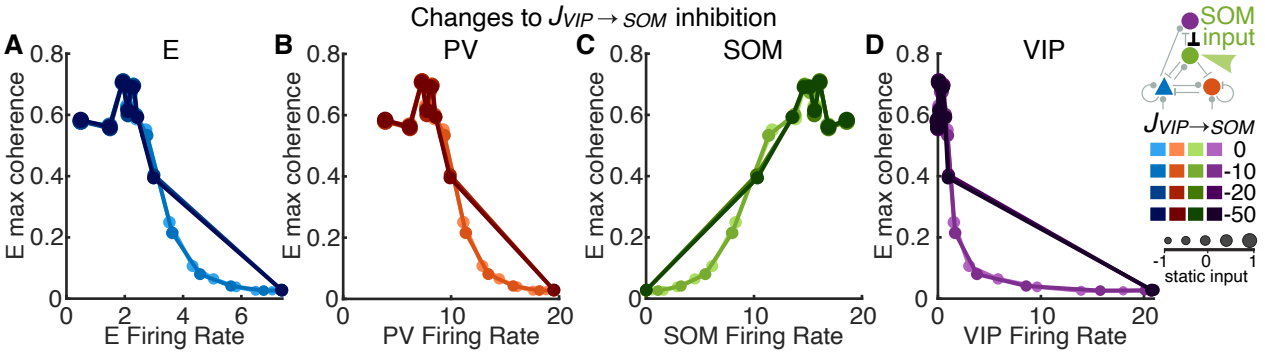

Figure S5: **VIP→SOM connection strength has little effect on modulation patterns. Related to Figures 5, 6.** Same format as Supplemental Figure S4. Static input was applied to SOM neurons. Modulation patterns are the same across VIP→SOM connection strengths $J_{VIP\to SOM}$ except for in the network with the largest strength (darkest color). Networks with large $J_{VIP\to SOM}$ become sensitive to small changes in external input to SOM. The firing rate of SOM neurons switches from zero to above 10 Hz and the rate of VIP neurons switches from about 20 Hz to near zero as input to SOM increases slightly (one step in panels C,D). Therefore, networks with large inhibition from VIP to SOM exhibit the WS state over only a limited parameter range and switch relatively abruptly between the SA and the SS states as input varies. Note that $J_{VIP\to SOM} = -10$ is the default circuit parameter used in the main text.

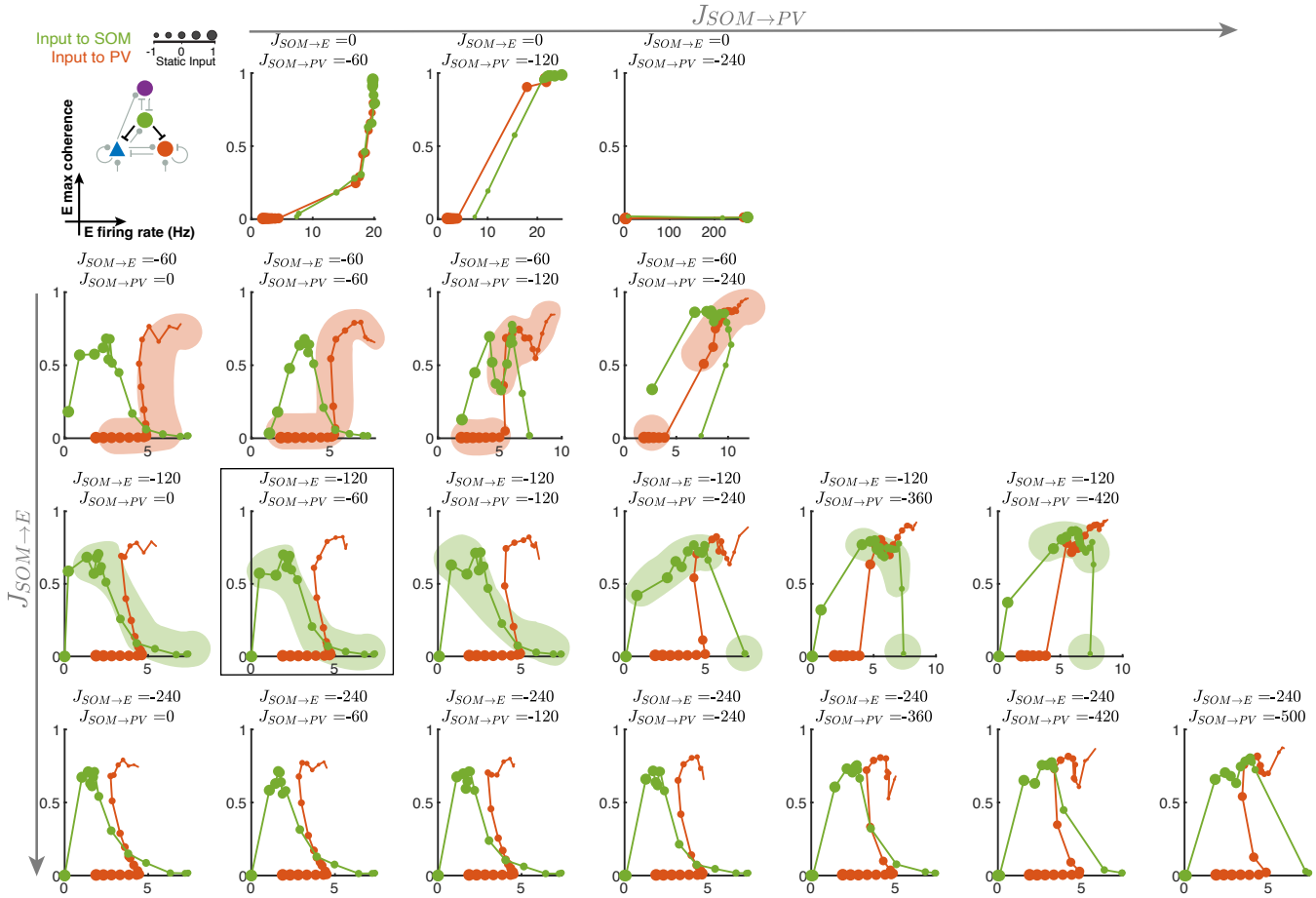

Figure S6: **Modulation patterns in networks with different SOM→E and SOM→PV connection strengths. Related to Figure 5.** Static input was either applied to PV neurons (red) or SOM neurons (green). Each plot represents the maximum coherence of E neurons versus the average firing rate of E neurons. Marker sizes correspond to increasing static input to the target population. Rows represent (negative) increases in synaptic connection strength of SOM→E. Columns represent (negative) increases in synaptic connection strength of SOM→PV. The boxed plot features the same parameters as the default network. We find that when $|J_{SOM\to E}| > |J_{SOM\to PV}|$ (lower triangle of the plots), the shapes of the modulation patterns for both input cases remain qualitatively consistent. When $|J_{SOM\to PV}|$ is much larger than $|J_{SOM\to E}|$, the network exhibits abrupt changes from the SA to the SS state, and the firing rate and coherence of E neurons tend to vary in the same direction over all levels of input to PV. The orange shading in row two and green shading in row three highlight examples of changes in modulation patterns as $|J_{SOM\to PV}|$ increases (across columns in the same row). Discontinuities in the shading are abrupt changes between adjacent dots (i.e., small changes in external input leading to large changes in coherence) along the modulation path.

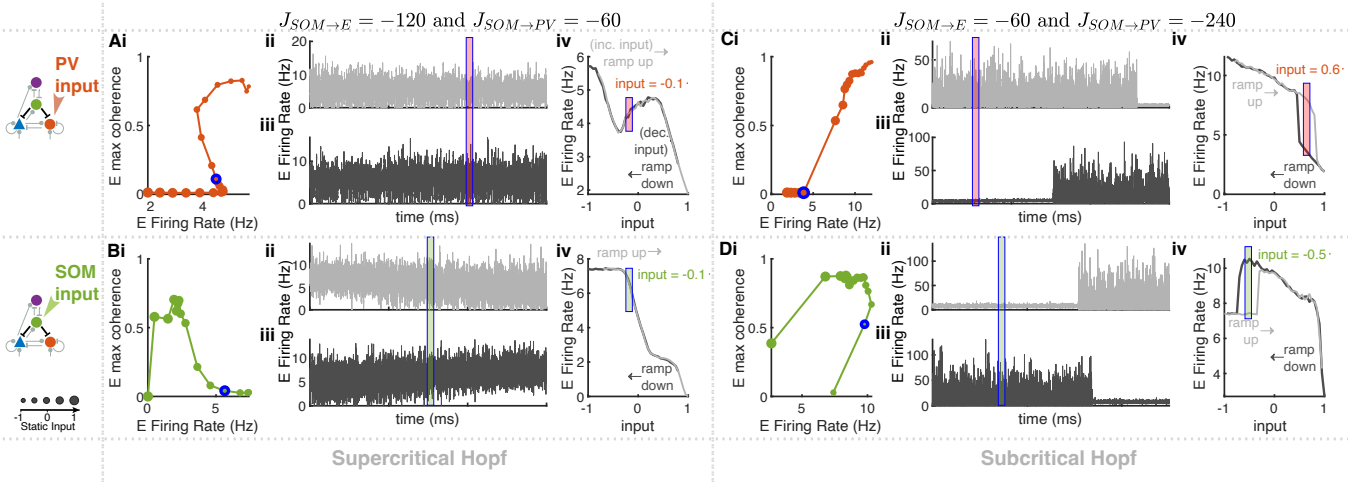

Figure S7: **Hysteresis effects in networks with strong SOM→PV inhibition in response to ramping input. Related to Figures 3,4,5.** (A,B) The default network ($J_{SOM\to E} = -120$ and $J_{SOM\to PV} = -60$; Figures 3,4) with input applied to PV (A) or SOM (B) neurons. (C,D) Same as A,B for a network with stronger SOM to PV inhibition ($J_{SOM\to E} = -60$, $J_{SOM\to PV} = -240$) with input applied to PV (C) or SOM (D) neurons. Panel (i): Modulation path of E population firing rates versus E maximum coherence with varying static input (same format as Figures 4A, S6). The blue outlined marker in (i) represents the input value that is indicated in panels (ii)-(iv) by colored rectangles. Note that each panel (i) was generated with a sequence of fixed values of static input to the indicated population, and not with ramping input, which changes in time. Panel (ii): The population-averaged firing rate of E neurons as a function of time with slowly increasing input (*ramp up* case). Panel (iii): same as panel (ii) for slowly decreasing input (*ramp down* case). In the ramping input cases, external inputs were increased or decreased by a small incremental change, ± 0.05, every 5 seconds. The 5-second interval allows sufficient time for the network to converge to a stationary state at the given input value. The colored rectangle in panels (ii) and (iii) indicates time intervals of the same input value in both ramping cases, which are aligned in time for comparison. Panel (iv): E population-average firing rates calculated within each 5-second interval of ramping input. The initial 250 ms of each interval was excluded to avoid transient activity. In the default network with $|J_{SOM\to E}| > |J_{SOM\to PV}|$ (A,B), the E firing rate is the same for each fixed input value in both *ramp up* and *ramp down* cases. This suggests that there is no co-existence of multiple network states for any input value and that the transition from the SA to the SS state is likely through a supercritical Hopf bifurcation where the amplitude of oscillation increases gradually after bifurcation. In contrast, in a network with $|J_{SOM\to E}| < |J_{SOM\to PV}|$ (C,D), the same input value results in different dynamic states in the *ramp up* and *ramp down* cases (Cii-Civ,Dii-Div, regions indicated by colored rectangles). This hysteresis effect demonstrates the co-existence of two network solutions, one asynchronous and one synchronous oscillation, over a range of input values. This suggests that oscillations arise via a subcritical Hopf bifurcation, where there is a sudden jump in the amplitude of oscillations after the bifurcation point, in networks with strong SOM→PV inhibition.

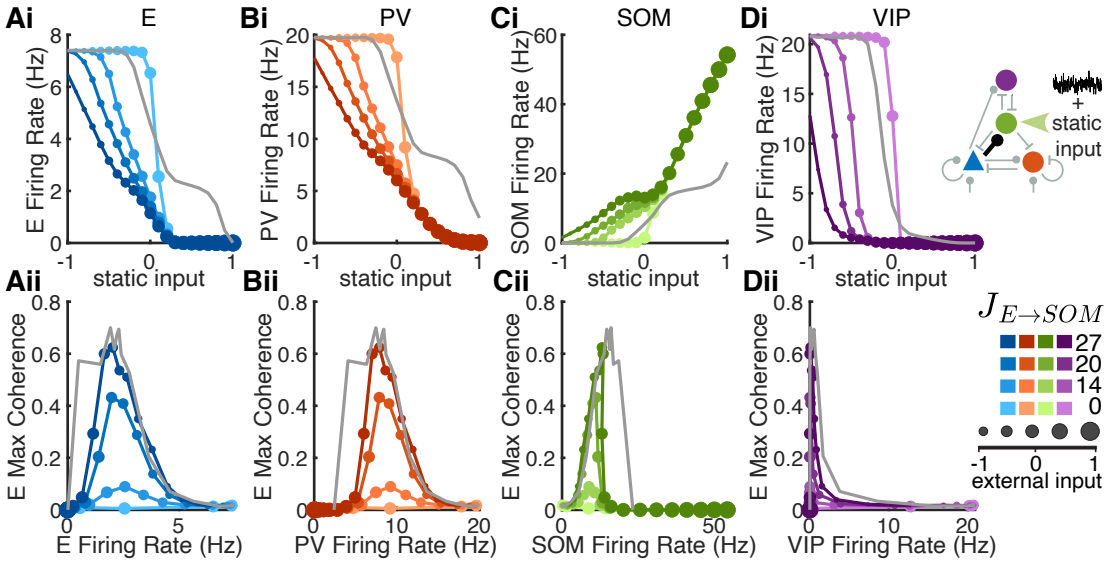

Figure S8: **Population rates and coherence in networks with different E→SOM connection strengths. Related to Figure 6.** Both static input and colored noise were applied to SOM neurons. The colored noise was constructed as an OU process to match the mean and variance of the recurrent excitatory input that SOM neurons receive in the default network without external input (same noise input as in Figure 6A,C). Static input varied from -1 to 1. Column: (A) E, (B) PV, (C) SOM, (D) VIP population. Row (i): Average firing rates of each cell population with respect to static input value. Row (ii): The maximum coherence of E neurons compared to the population firing rates of each cell type. The grey curves are from the default network ($J_{E\to SOM} = 27$), with SOM neurons receiving static input without the OU noise.

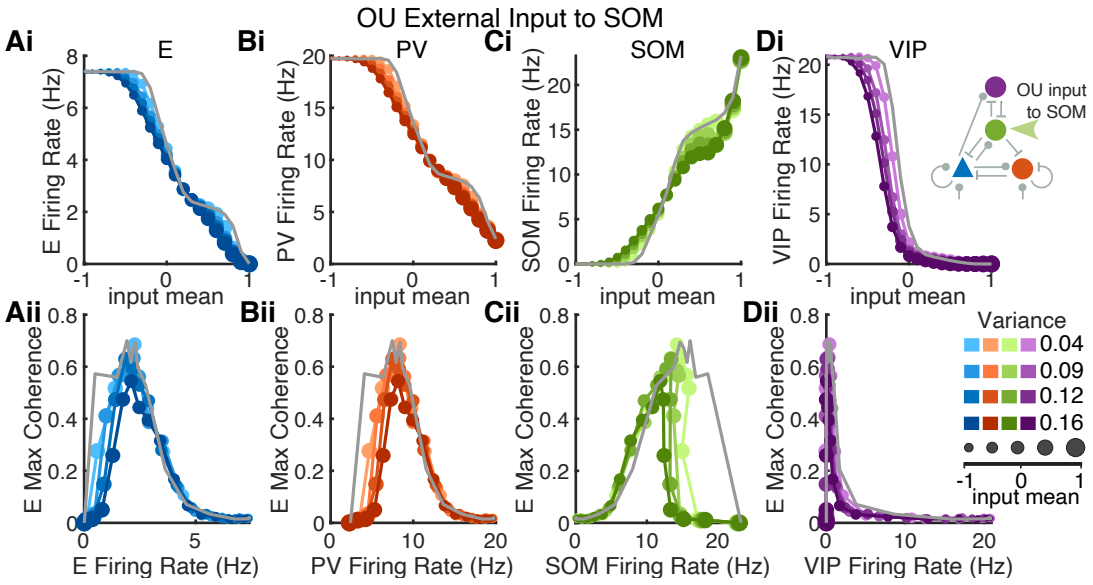

Figure S9: **Weak impacts of dynamic noise input parameters on population rates and coherence. Related to Figure 7.** Independent temporally-varying noise, modeled as an OU process of given mean (dot size) and variance (color shade), is applied to each SOM neuron. Columns show firing rate and coherence of (A) E, (B) PV, (C) SOM, (D) VIP populations. Row (i): Average firing rate of each cell population with respect to the mean value of OU input. Row (ii): The maximum coherence of E neurons compared to the population firing rates of each cell type. The grey curves are from the default network with SOM receiving static input.

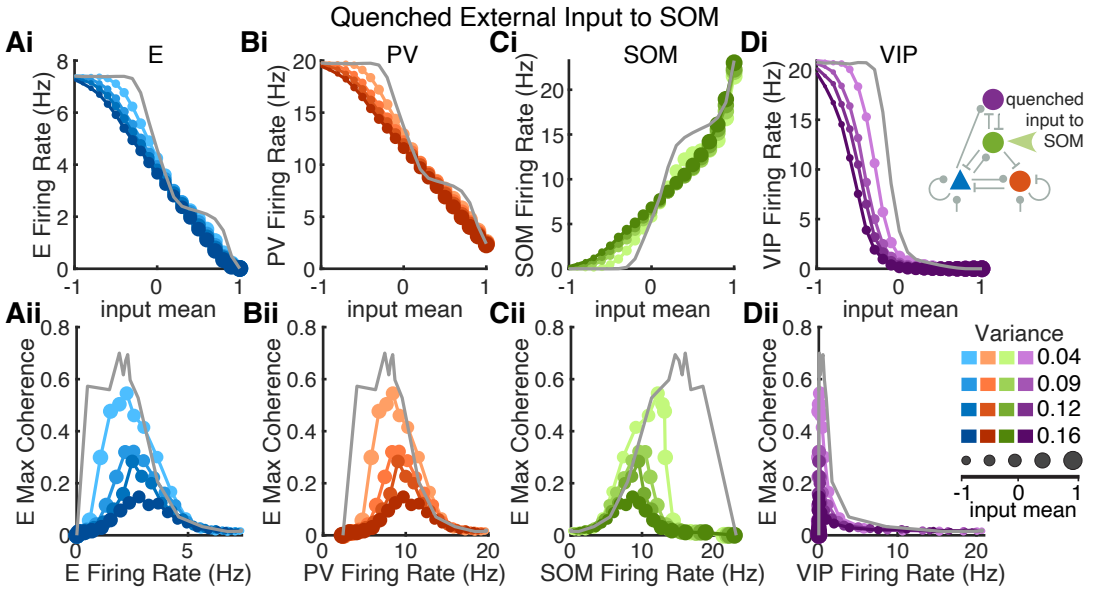

Figure S10: **Impacts of quenched inputs on population rates and coherence. Related to Figure 7.** Quenched input is spatially variable, but temporally invariant. Each SOM neuron receives an input value that is sampled from a Gaussian distribution with given mean (dot size) and variance (color shade). Columns show firing rate and coherence of (A) E, (B) PV, (C) SOM, (D) VIP populations. Row (i): Average firing rate of each cell population with respect to the mean value of the quenched input. Row (ii): The maximum coherence of E neurons compared to the population rates of each cell type. The grey curves are from the default network with SOM receiving static input.

Supplementary Video 1: Spiking activities of the spatially dependent spiking neuron network in the subcircuit asynchronous (SA) state (same parameters as in Figure 2A). Each dot indicates that the neuron at spatial position (x, y) fired within one millisecond of the time stamp shown on top. Color of each dot indicates the cell type of the neuron that fired (blue: E; red: PV; green: SOM; purple: VIP).

Supplementary Video 2: Same as Video 1 for the network in the weakly synchronous (WS) state (same parameters as in Figure 2B).

Supplementary Video 3: Same as Video 1 for the network in the strongly synchronous (SS) state (same parameters as in Figure 2C).